OPEN ACCESS

University of BRISTOL

Altenau, E. H., Pavelsky, T. M., Bates, P. D., & Neal, J. C. (2017). The effects of spatial resolution and dimensionality on modeling regional-scale hydraulics in a multichannel river. *Water Resources Research*, *53*(2), 1683–1701. https://doi.org/10.1002/2016WR019396

Publisher's PDF, also known as Version of record

Link to published version (if available):
10.1002/2016WR019396

Link to publication record in Explore Bristol Research
PDF-document

This is the final published version of the article (version of record). It first appeared online via Wiley at http://onlinelibrary.wiley.com/doi/10.1002/2016WR019396/full . Please refer to any applicable terms of use of the publisher.

University of Bristol - Explore Bristol Research
General rights

This document is made available in accordance with publisher policies. Please cite only the published version using the reference above. Full terms of use are available:
http://www.bristol.ac.uk/red/research-policy/pure/user-guides/ebr-terms/

AGU PUBLICATIONS

Water Resources Research

RESEARCH ARTICLE
10.1002/2016WR019396

The effects of spatial resolution and dimensionality on modeling regional-scale hydraulics in a multichannel river

Elizabeth H. Altenau[1], Tamlin M. Pavelsky[1], Paul D. Bates[2], and Jeffrey C. Neal[2]

[1]Department of Geological Sciences, University of North Carolina, Chapel Hill, North Carolina, USA, [2]School of Geographical Sciences, University of Bristol, Bristol, UK

Key Points:
- We validate a simple, raster-based model's ability to simulate 2-D hydraulics in a multichannel river
- For 1-D model formulations, simplifications to the multichannel morphology dominate model errors
- Inclusion of the anabranching network is essential for simulating proper hydraulics at regional scales

Correspondence to:
E. H. Altenau,
ealtenau@unc.edu

Citation:
Altenau, E. H., T. M. Pavelsky, P. D. Bates, and J. C. Neal (2017), The effects of spatial resolution and dimensionality on modeling regional-scale hydraulics in a multichannel river, *Water Resour. Res.*, *53*, doi:10.1002/2016WR019396.

Received 22 JUN 2016
Accepted 5 FEB 2017
Accepted article online 9 FEB 2017

Abstract As modeling capabilities at regional and global scales improve, questions remain regarding the appropriate process representation required to accurately simulate multichannel river hydraulics. This study uses the hydrodynamic model LISFLOOD-FP to simulate patterns of water surface elevation (WSE), depth, and inundation extent across a ~90 km, anabranching reach of the Tanana River, Alaska. To provide boundary conditions, we collected field observations of bathymetry and WSE during a 2 week field campaign in summer 2013. For the first time at this scale, we test a simple, raster-based model's capabilities to simulate 2-D, in-channel patterns of WSE and inundation extent. Additionally, we compare finer resolution ($\leq$25 m) 2-D models to four other models of lower dimensionality and coarser resolution (100–500 m) to determine the effects of simplifying process representation. Results indicate that simple, raster-based models can accurately simulate 2-D, in-channel hydraulics in the Tanana. Also, the fine-resolution, 2-D models produce lower errors in spatiotemporal outputs of WSE and inundation extent compared to coarse-resolution, 1-D models: 22.6 cm versus 56.4 cm RMSE for WSE, and 90% versus 41% Critical Success Index values for simulating inundation extent. Incorporating the anabranching channel network using subgrid representations for smaller channels is important for simulating accurate hydraulics and lowers RMSE in spatially distributed WSE by at least 16%. As a result, better representation of the converging and diverging multichannel network by using subgrid solvers or downscaling techniques in multichannel rivers is needed to improve errors in regional to global-scale models.

1. Introduction

Hydrodynamic modeling is a useful tool for predicting the spatially distributed water surface elevations (WSEs) needed for estimating flood magnitude, extent, and timing, especially in areas where field data are sparse and river morphologies are complex [*Bates and De Roo*, 2000; *Horritt and Bates*, 2001; *Hunter et al.*, 2007; *Beighley et al.*, 2009; *Bates et al.*, 2010; *Neal et al.*, 2012a, 2012b; *Nguyen et al.*, 2015]. Research over the past few decades has shown that models with simplified approximations of flow perform well and produce accurate estimates of WSE and inundation extent compared to more complex solutions of the full shallow water equations [*Bates and De Roo*, 2000; *Bradbrook et al.*, 2004; *Neal et al.*, 2012b; *de Almeida and Bates*, 2013]. Additionally, advances in remote sensing observations of key hydraulic variables have allowed substantial developments in implementing hydrodynamic models at regional to global scales [*Paiva et al.*, 2011, 2013; *Yamazaki et al.*, 2011; *Sampson et al.*, 2015, *Schumann et al.*, 2016]. Despite recent progress, the need to balance spatiotemporal resolution, computational efficiency, and data availability limits regional-scale flood models spanning river lengths $\geq$100 km to using downscaling techniques, subgrid representations, and 1-D routing schemes to simulate channel flows [*Cloke and Pappenberger*, 2009; *Bierkens et al.*, 2015; *Sampson et al.*, 2015]. This requisite level of simplicity may limit the accuracy of model outputs, especially in rivers that are not well represented in 1-D, such as multichannel systems. Such environments are quite common. *Allen and Pavelsky* [2015] observe that for the North American continent multichannel river systems make up approximately 26% of Landsat-observable rivers above 60°N, and *Latrubesse et al.* [2008] demonstrate that many of the world's largest river systems display anabranching morphologies.

To date, the most common approaches to regional-scale hydrodynamic modeling have not been rigorously tested in multichannel systems due to these rivers' challenging dynamics. There is extensive research using detailed 2-D and 3-D models at scales of 1–30 km to simulate the hydraulics and morphodynamics of

© 2017. American Geophysical Union. All Rights Reserved.

multichannel rivers [*Bridge*, 1993; *Lane and Richards*, 1998; *Lane et al*., 1999; *Nicholas and Sambrook Smith*, 1999; *Nicholas et al*., 2012; *Williams et al*., 2013; *Ziliani et al*., 2013]. However, practical application of these models across hundreds of kilometers, much less globally, is computationally infeasible due to the need for fine-grid scales and full solutions to the Saint Venant or Navier-Stokes equations [*Bates et al*., 2005]. Decision makers need efficient models of multichannel rivers at regional scales in order to predict flood patterns, which threaten people and valuable infrastructure within these highly complex river environments.

An important question that arises is one of appropriate complexity: How simple can we make a regional-scale model of a multichannel system and still produce useful information for science or management? Simpler model formulations reduce computational burden, increase viable domain sizes, and improve the feasibility of ensemble modeling. Previous research has explored the effects of spatial resolution and model dimensionality independent of one another on both single-thread and multichannel rivers [*Lane et al*., 1999; *Horritt and Bates*, 2001, 2002; *Horritt et al*., 2006; *Nicholas et al*., 2012; *Schubert et al*., 2015; *Javernick et al*., 2016]. To the best of our knowledge, however, no previous work has explored the effects of both model resolution and dimensionality on a multichannel river at the scale of ~100 km or more. Fortunately, advances in algorithms, data availability, and computational resources now allow us to address this question, as we can build fine-resolution (≤25 m) models of 100 km+ reaches that can resolve all river channels explicitly [*Schubert et al*., 2015]. These fine-resolution models can act as benchmarks against which we assess how simplifications to the bifurcating and converging channel network affect modeling flood wave propagation, water level, and inundation extent in multichannel systems at regional to global scales.

In order to address these questions, we compare six different LISFLOOD-FP models along a ~90 km, multichannel reach of the Tanana River, Alaska. For the first time in a highly complex, anabranching river, we test how well a simple, raster-based model can simulate 2-D channel flows by assessing temporal and spatial outputs of WSE and inundation extent at the ~100 km reach scale. We then compare the 2-D models to several models of lower dimensionality and coarser resolution. Simulations range from a 10 m resolution, 2-D model that fully captures the river's complexity to a 500 m resolution 1-D model that substantially simplifies the overall river structure. We focus on addressing (1) how well a simple, raster-based model can simulate 2-D channel hydraulics and (2) how degrading the physical representation of a multichannel river system affects spatial and temporal errors in model outputs.

2. Hydrodynamic Model

For this study we use the raster-based, hydrodynamic model LISFLOOD-FP [*Bates and De Roo*, 2000; *Bates et al*., 2010; *de Almeida et al*., 2012; *Neal et al*., 2012a]. LISFLOOD-FP uses an explicit finite difference scheme to simulate shallow water waves over a staggered grid using a local inertial approximation of the 1-D Saint-Venant or shallow water equations [*Cunge et al*., 1980]

$$\frac{\partial A}{\partial t}+\frac{\partial Q}{\partial x}=0, \tag{1}$$

$$\underbrace{\frac{\partial Q}{\partial t}}_{\text{acceleration}}+\underbrace{\frac{\partial}{\partial x}\left(\frac{Q^2}{A}\right)}_{\text{advection}}+\underbrace{\frac{gA\partial(h+z)}{\partial x}}_{\text{water slope}}+\underbrace{\frac{gn^2Q^2}{R^{\frac{4}{3}}A}}_{\text{friction slope}}=0, \tag{2}$$

where equation (1) describes the continuity of mass and equation (2) the continuity of momentum such that $Q[L^3T^{-1}]$ is the discharge, $A[L^2]$ is the flow cross section, $g[LT^{-2}]$ is the acceleration due to gravity, $R[L]$ is the hydraulic radius, $h[L]$ is the water depth, $z[L]$ is the bed elevation, $n[TL^{-1/3}]$ is the Manning friction coefficient, $x[L]$ is the longitudinal coordinate, and $t[T]$ is the time. The local inertial formulation incorporates the friction slope, water slope, and local acceleration terms from the momentum equation of the shallow water equations above but neglects advection because bed friction tends to dominate over advective processes for large length scales [*Hunter et al*., 2007]. Inclusion of local acceleration allows for faster computations with increased stability compared to simpler diffusive wave models [*Bates et al*., 2010; *de Almeida et al*., 2012; *Neal et al*., 2012a].

For model resolutions ≤100 m we represent the channel bathymetry directly in the model grid and compute the time evolution of flow over this complex surface in 2-D (Figures 1a and 1d). This study tests LISFLOOD-FP's ability to simulate 2-D channel flows in a multichannel river environment for the first time.

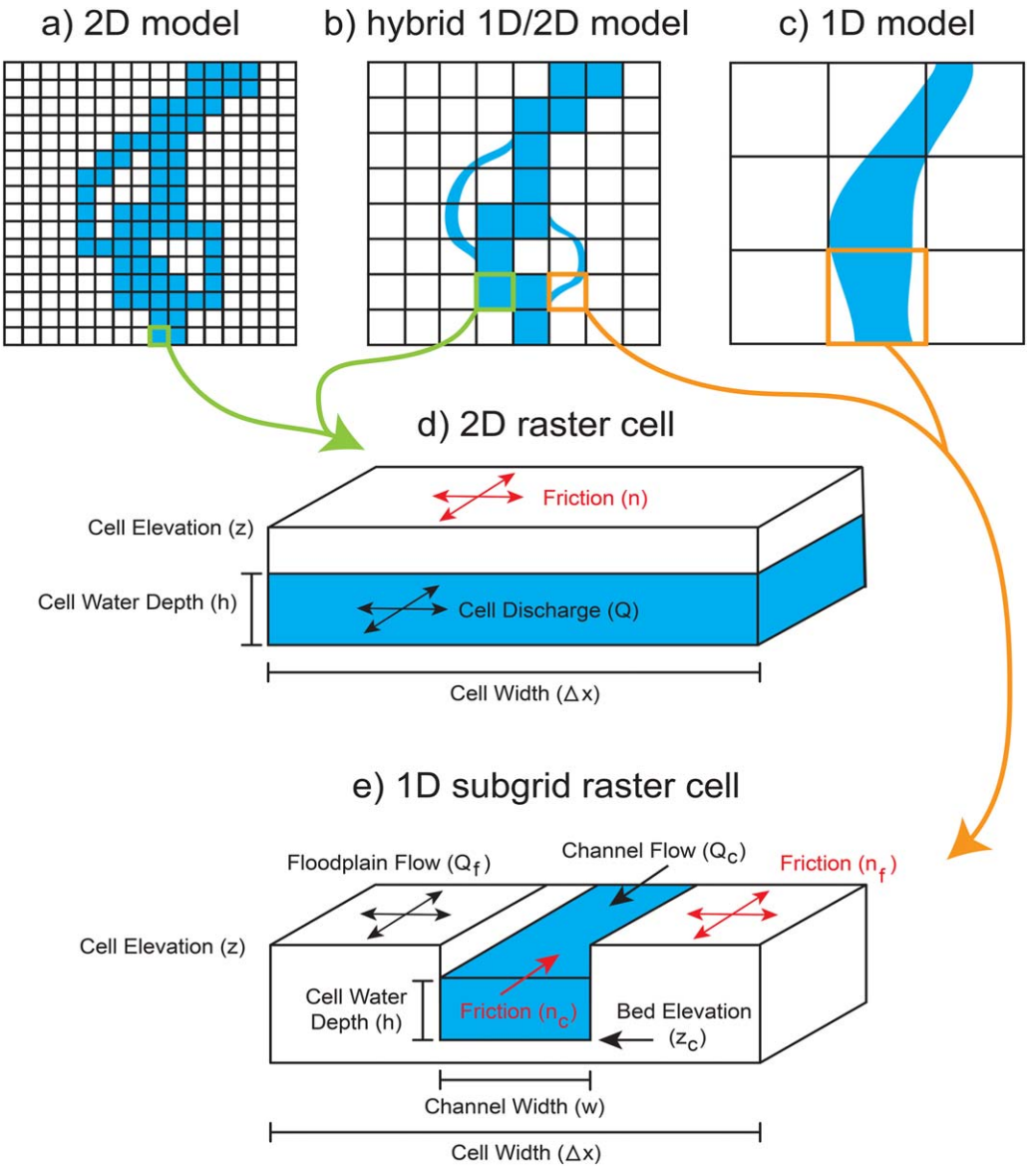

Figure 1. Conceptual schematic of (a) 2-D channel flow model, (b) hybrid 1-D/2-D channel flow model, (c) 1-D channel flow model, (d) 2-D raster cell with relevant variables, and (e) 1-D subgrid raster cell with relevant variables.

To do so, LISFLOOD-FP simultaneously solves the continuity of mass and momentum equations. The continuity equation for a raster cell over a time step Δt is

$$h_{i,j}^{t+\Delta t} = h_{i,j} + \Delta t \frac{Q_{x\ i-1/2,j}^{t+\Delta t} - Q_{x\ i-1/2,j}^{t+\Delta t} + Q_{y\ i-1/2,j}^{t+\Delta t} - Q_{y\ i-1/2,j}^{t+\Delta t}}{A_{i,j}}, \quad (3)$$

where Q is the flow between cells, h is the cell water depth, A is the cell area, and the subscripts i and j are cell indices in the x and y directions [*Neal et al.*, 2012a]. For the momentum equation, flows in the x and y directions are decoupled and solved using the same calculation. The momentum equation for flow Q between raster cells in the x direction is

$$Q_{i+1/2}^{t+\Delta t} = \frac{q_{i+1/2}^{t} - g h_{flow}^{t} \Delta t S_{i+1/2}^{t}}{\left[1 + g\Delta t n^2 |q_{i+1/2}^{t}| / \left(h_{flow}^{t}\right)^{7/3}\right]} \Delta x, \quad (4)$$

where Δx is the cell width, g is acceleration due to gravity, q^t is flow from the previous time step Q^t divided by cell width Δx, S is water slope between cells, n is the Manning friction coefficient, and h_{flow} is the depth between cells which water can flow [*Neal et al*., 2012a]. To maintain stability, the model uses a time-stepping equation based on the Courant-Friedrichs-Lewy condition [*Courant et al*., 1928] and is limited to

$$\Delta t = \alpha \frac{x}{\sqrt{\max(h^t) g}}, \tag{5}$$

where $\max(h^t)$ is the maximum water depth in the model domain and α is a stability coefficient that ranges from 0.2 to 0.7 for most floodplains. As the grid size decreases, the time step scales with $1/\Delta x$ [*Bates et al*., 2010; *Neal et al*., 2012a].

As the model spatial resolutions increase to $\geq$100 m, the grid scale imposes an increasingly severe restriction on the simulation of channelized flows, and we therefore treat channels as subgrid-scale features using the approach of *Neal et al*. [2012a]. Here flow in channels narrower than the grid resolution are simulated using a 1-D interpretation of the same local inertial formulation used for the 2-D scheme with two additional variables that represent the channel bed elevations (z_c) and channel widths (w) (Figures 1b, 1c, and 1e) [*Neal et al*., 2012a; *Schumann et al*., 2014a; *Sampson et al*., 2015]. This approach is adopted because an explicit representation of channels is known to be important for connectivity and water partitioning in floodplain dynamics [*Neal et al*., 2012a; *Sampson et al*., 2015].

The primary inputs for the models are floodplain topography, bathymetry, roughness parameters, discharge, and stage information. LISFLOOD-FP is suitable for gradually varied flow and can become unstable at low Manning's n values (less than 0.01) or under supercritical flow conditions [*Bates et al*., 2010; *Neal et al*., 2012b; *de Almeida and Bates*, 2013]; however, these conditions do not arise in our study reach for the model resolutions that we use. We chose LISFLOOD-FP as an appropriate model for this study because it is computationally efficient, can simulate flows in multiple dimensions, and is widely used within the hydrodynamic modeling community.

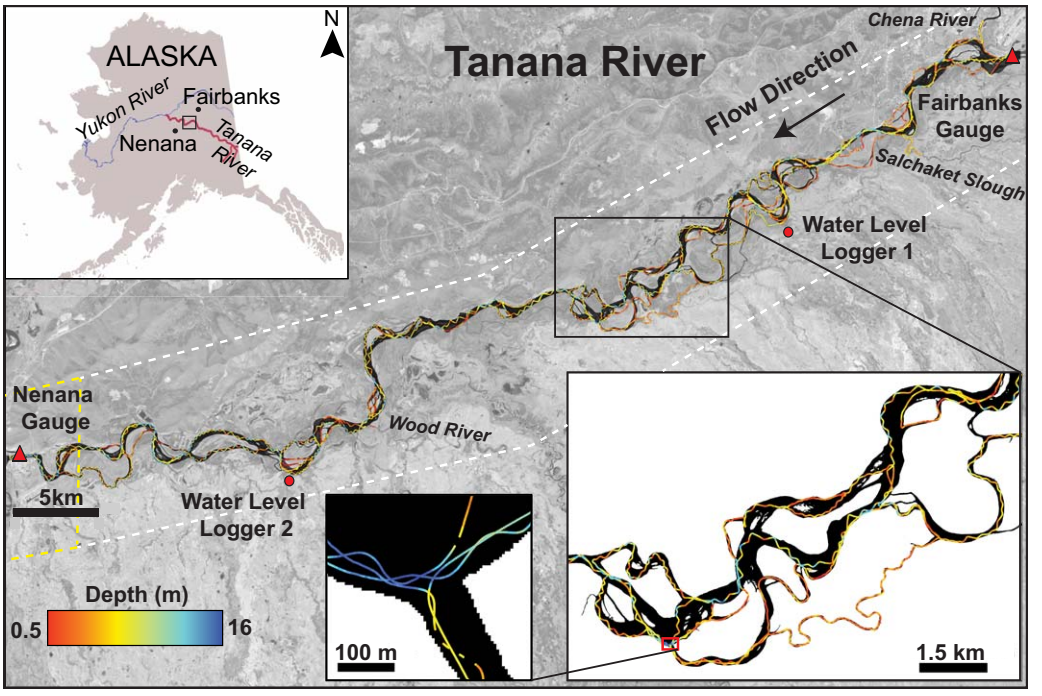

Figure 2. Location of the Tanana River shown using a Landsat 8 satellite image acquired on 18 June 2013. Bathymetric observations collected using a single-beam echo sounder during a field campaign between 1 July 2013 and 8 July 2013 are color coded along the river with close-up insets for detail. Locations of the USGS gauge stations (red triangles), internal water level loggers (red circles), and major tributaries are shown. RapidEye imagery extents used to create the river mask for the custom interpolation are shown for 12 July 2013 in the white dashed lines and 28 May 2013 in the yellow dashed lines.

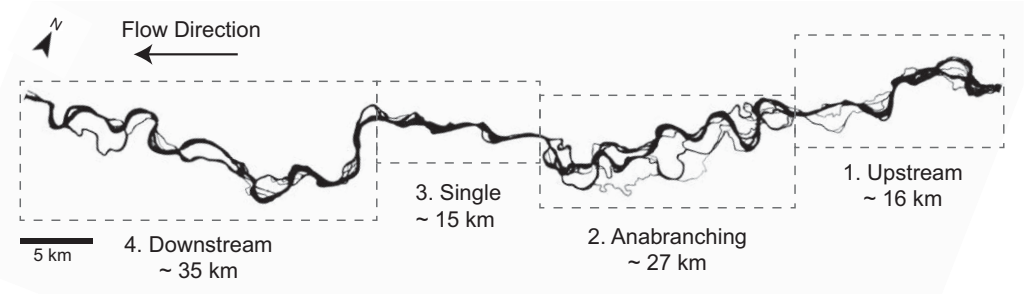

Figure 3. Extent of predefined subreaches used to calculate error statistics in the profile analysis.

3. Study Site

We chose a ~90 km reach of the Tanana River in Alaska between the towns of Fairbanks and Nenana to assess the effects of model resolution and dimensionality on multichannel river hydraulics (Figure 2). The Tanana drains a large swath of the eastern Alaska Range and central Alaskan highlands, flowing northwest until it joins with the Yukon River. The shape of the annual hydrograph is largely determined by melt of snowpack and glaciers during the spring and summer. Low flows in the winter lead to a rapid increase of flow during the springtime and peak flows during the summer. Mean discharge during the open water season (May–October) for the Tanana is ~1299 m^3/s according to records from the USGS station at Nenana (Station Number: 15515500) from 1962 to 2013. Field calculations and modeling performed by *Toniolo et al.* [2010] indicate flows along the Tanana are gradually varied and subcritical with an average Froude number of 0.30 along the Thalweg and are therefore suitable for modeling with LISFLOOD-FP.

The Tanana's glacial origin results in a high sediment load, which interacts with local topography to produce a complex morphology that ranges from highly braided to a single meandering channel. The suspended sediment load in the Tanana is extremely high (an estimated 33 metric tons per year) and consists primarily of silt and clay. For comparison, the farthest downstream station on the Yukon River recorded an estimated 68 metric tons of suspended sediment per year with a mean annual discharge of ~6428 m^3/s [*Brabets et al.*, 2000; *Dornblaser and Striegl*, 2009]. The bed of the Tanana, composed of sand and gravel, is quite mobile, which results in comparatively rapid changes in channel planform. Physiographic characteristics of the region include alluvial deposits and discontinuous permafrost [*Brabets et al.*, 2000].

The study reach contains multiple morphologies ranging from a single channel to as many as eight different channels in a cross section. It is an ideal site for this research because of its diverse morphology and because it is bounded by two USGS gauge stations needed for model boundary conditions (Figure 2). We define several subreaches based on changes in river morphology (Figure 3). The first 16 km of the reach contains a primary main channel with an average width of ~450 m and smaller sloughs no wider than 100 m. Most of the flow is carried by the large main channel (Figure 3(1)). In the next 27 km of the river, flow is partitioned into many anabranching channels ranging from 20 to 240 m wide that divert more of the flow around the main channel (Figure 3(2)). About halfway through the study reach the anabranching channels converge into a single channel due to bedrock bluffs to the north. This reach continues for 15 km and only contains two small sloughs in addition to the main stem. Therefore, we expect this portion of the reach to behave hydraulically much like a single channel (Figure 3(3)). The final 35 km subreach returns to a planform with several channels but remains more confined and less complex than the upstream anabranching subreach (Figure 3(4)).

4. Model Setup

4.1. Existing Data Sets

Data sets needed to build the models tested here include a fine-resolution digital elevation model (DEM), bathymetry, and hydrometric information including river discharge and stage. We use an Alaska interferometric synthetic aperture radar (IfSAR) DEM (http://ifsar.gina.alaska.edu/) with 5 m resolution for the floodplain topography. Mean vertical accuracy of the Alaska IfSAR products is 3 m, and the horizontal accuracy is 12.2 m. Errors in the floodplain topography are a low concern since the primary focus of this study is on in-

channel hydraulics, and very little of the floodplain topography is inundated in our simulations. Discharge and stage records at 15 min intervals from USGS gauge stations in Fairbanks and Nenana, Alaska provide model boundary conditions. The upstream boundary consists of time-varying discharge information, and the downstream boundary is a time series of stage. We add point-source discharge to the model at two locations to represent the Chena River and Salchaket Slough, which are inflowing tributaries. Salchaket Slough is a ~50 km long subchannel of the Tanana River that splits from the main channel upstream of the Fairbanks gauge station and reenters below it. For the Chena River, we use USGS discharge records from a gauge station ~15 km upstream of the confluence with the Tanana. The distance between the Chena gauge station and the Tanana River confluence is unlikely to affect the model simulations because there are no inflowing point sources along the Chena between the gauge and the Tanana. Additionally, the Chena River flood wave's transit time is relatively small compared to the dynamics of the Tanana River flood wave. Salchaket Slough does not have a gauge station, so we estimate discharge based on in situ measurements acquired with a Sontek M9 acoustic Doppler current profiling (ADCP) system (http://www.sontek.com/productsdetail.php?RiverSurveyor-S5-M9-14) during a separate field campaign on 8 June 2015. To measure discharge, we set up a cableway across Salchaket Slough just upstream of its confluence with the Tanana River. Six discharge measurements acquired between 3:15 P.M. and 3:30 P.M. ranged from 90.29 to 94.01 m^3/s, with an average discharge of 91.48 m^3/s. On this date, Salchaket Slough was contributing 14% of the downstream discharge observed at the Nenana gauge station, and we assume that this percentage is constant in time. Adding discharge inputs from the Chena River and Salchaket Slough results in an average difference of 1% between the discharge records at the Fairbanks and Nenana model boundaries, thereby effectively closing the reach mass balance. We assume the discharge measurements are error-free, but in reality they are likely to have errors ranging between ±6 and ±19% [*Harmel et al*., 2006; *Di Baldassarre and Montanari*, 2009; *Bates et al*., 2013]. Reported channel conditions from USGS field measurements at the upstream boundary of our study site during the duration of our model simulations (July–September 2013) are described as follows: *Channel stability* (Firm), *channel material* (sand and gravel), and *Channel evenness* (Even) (http://waterdata.usgs.gov/nwis/measurements). Based on these USGS reports and the increased likelihood that the Tanana River is subject to morphological changes, we estimate the discharge uncertainty in our model ranges between ±10% and ±20% [*Harmel et al*., 2006]. Therefore, the actual uncertainty in discharge is probably considerably larger than the 1% discrepancy between the two gauges resulting from our analysis. Remaining discrepancies can likely be attributed to groundwater interactions with the river and other much smaller tributary inputs.

4.2. Field Measurements

Detailed bathymetric information is necessary to implement the 2-D models. We collected measurements of channel bathymetry and WSE during a 2 week field campaign from 29 June 2013 through 13 July 2013. In total, we collected depth and WSE at ~220,000 points using a single-beam SonarMite Echo Sounder v.3.0 and Trimble R9 survey-grade GPS system (Figure 2). Using a side-scanning sonar system was unfeasible due to high costs and risk of damage to the equipment in the harsh conditions of the Tanana River. We mounted the echo sounder and GPS unit on the right stern of a 28 foot aluminum-hulled riverboat. The transducer was placed perpendicular to the water surface and submerged 0.18 m below the surface. Reported accuracy for the SonarMite Echo Sounder is ±0.025 m (http://www.ohmex.com/sonarmite.html). We were unable to compensate for roll or heave motion from the boat because the GPS antennas we had access to did not have National Marine Electronics Association (NMEA) capabilities. We took precautions to minimize roll and heave motions by traveling at a low speed of ~15 mph, though vessel motion likely increases uncertainty in the depth measurements.

We set the echo sounder and GPS to record every 0.5 s and matched bathymetric point observations to associated GPS locations using the recorded time stamps. To estimate error in the depth and WSE measurements, we identified 914 crossover point pairs in the observations within a 0.10 m radius of each other and calculated root mean square error (RMSE) for depth and WSE. RMSE for depth observations is 0.267 m and RMSE for WSE observations is 0.162 m. Bias is very small for both the depths and WSEs at −0.017 and 0.016 m, respectively. In addition to the bathymetry collection, we installed two Solinst pressure transducer water level loggers (solinst.com) at ~23 and ~70 km downstream of Fairbanks (Figure 2). We used differential GPS and WSE surveys to achieve an elevation accuracy of ±4 cm at the water logger sites. The water loggers recorded stage information at 5 min intervals from the start of our field campaign on 29 June 2013

through early September. We converted stage values to WSE by using an optical survey level and stadia rod to measure the difference between the water surface at the logger sites and GPS survey benchmarks on the banks of the river near the water loggers.

4.3. 2-D Channel Topography

We develop a custom interpolation method to transform the irregularly spaced bathymetric point data into a raster grid (Figure 4). Isotropic interpolation methods available in ArcGIS and similar software do not produce hydrologically intuitive bathymetric patterns due to the anisotropic flow direction characteristic of rivers. We considered using other river-based interpolation methods that account for flow direction. The most common methods involve tailored search radii that utilize the anisotropic shape of a river cross-section [*Osting*, 2004], or channel-based coordinate systems guided by a channel centerline [*Smith and McLean*, 1984; *Goff and Nordfjord*, 2004; *Merwade et al*., 2005, 2006, 2008; *Legleiter and Kyriakidis*, 2006, 2008; *Merwade*, 2009]. These methods are suitable for sinuous, single-channel systems where one centerline is applicable [*Smith and McLean*, 1984]. Extreme sinuosity, significant changes in direction, and braided channels are problematic for interpolation methods using channel-based coordinate systems [*Goff and Nordfjord*, 2004; *Legleiter and Kyriakidis*, 2008; *Merwade et al*., 2008]. Implementing a standard channel transformation in a river like the Tanana that contains multiple flow centerlines and directions within a cross section would require extensive manual work or multiple coordinate transformations and were thus discarded. The custom interpolation used for this study combines image processing techniques with similar concepts used in traditional channel transformations to adapt the search radius to interpolate points in the general flow directions of a multichannel river with little manual input.

Inputs needed for the interpolation are a set of channel centerlines calculated using the RivWidth software package [*Pavelsky and Smith*, 2008], a river mask, and the bathymetric point observations in TIFF format (Figure 4a). First, we create the river mask using 5 m resolution RapidEye imagery (http://www.satimagingcorp.com/satellite-sensors/other-satellite-sensors/rapideye/) acquired during the week of the field campaign on 12 July 2013 (Figure 2). The only exception is the image used for the westernmost seven kilometers of the study reach, which was acquired 3 months earlier in May 2013 (Figure 2). This portion of the river covered by the older RapidEye image is constrained by tall bedrock bluffs, so the planform of the river is unlikely to have changed substantially between May and our field campaign in July. We extract river inundation extent by thresholding a normalized difference water index (NDWI) transformation of the imagery [*McFeeters*, 1996]. To correct for areas near the riverbanks that are identified as river in the floodplain DEM and not in the imagery, we add these areas to the river mask. This correction is necessary to prevent interpolation artifacts in the DEM river surface from creating large errors in the model outputs, and the additional area accounts for a very small percentage (4.2%) of the total river surface area. We apply RivWidth to the river mask in order to create the channel centerline image needed for the interpolation, which consists of centerlines for every channel along the reach (Figure 4a). The interpolation code uses the centerline image to create regions parallel to the centerlines that represent the river's general flow orientation. These areas are defined by the distance from the centerline and are used to identify the optimal observations needed for interpolation (Figure 4b). We refer to these divisions as the distance-from-centerline (DFC) regions. The code identifies bathymetric point observations that fall within a defined radius of each river mask pixel and the DFC region of the pixel (Figure 4c). If a minimum number of observational points are not found within the DFC region and the specified radius, the search algorithm expands to include observations in adjacent DFC regions (Figure 4d). For this interpolation, we choose a search radius of 500 m and a minimum number of eight bathymetric observations. Once the minimum number of points is identified, the algorithm uses an inverse distance weighting (IDW) interpolation method (Figure 4e). The IDW formula to predict the bathymetric elevation for a given pixel location of unknown value is

$$\hat{Z}(l_0) = \sum_{i=1}^{n} w_i Z(l_i), \tag{6}$$

where $\hat{Z}(l_0)$ is the predicted elevation for a given location (l_0), n is the number of observed sample points surrounding the prediction location, $Z(l_i)$ is the observed elevation value at location (l_i), and w_i are the weights assigned to each observed elevation point determined by the following formula:

$$w_i = \frac{d_{i0}^{-p}}{\sum_{i=1}^{n} d_{i0}^{-p}}. \tag{7}$$

For greater distances, the weight is reduced by a factor of p, which we assign a value of five, and d_{i0} is the distance between the predicted location and each of the observed locations. This process

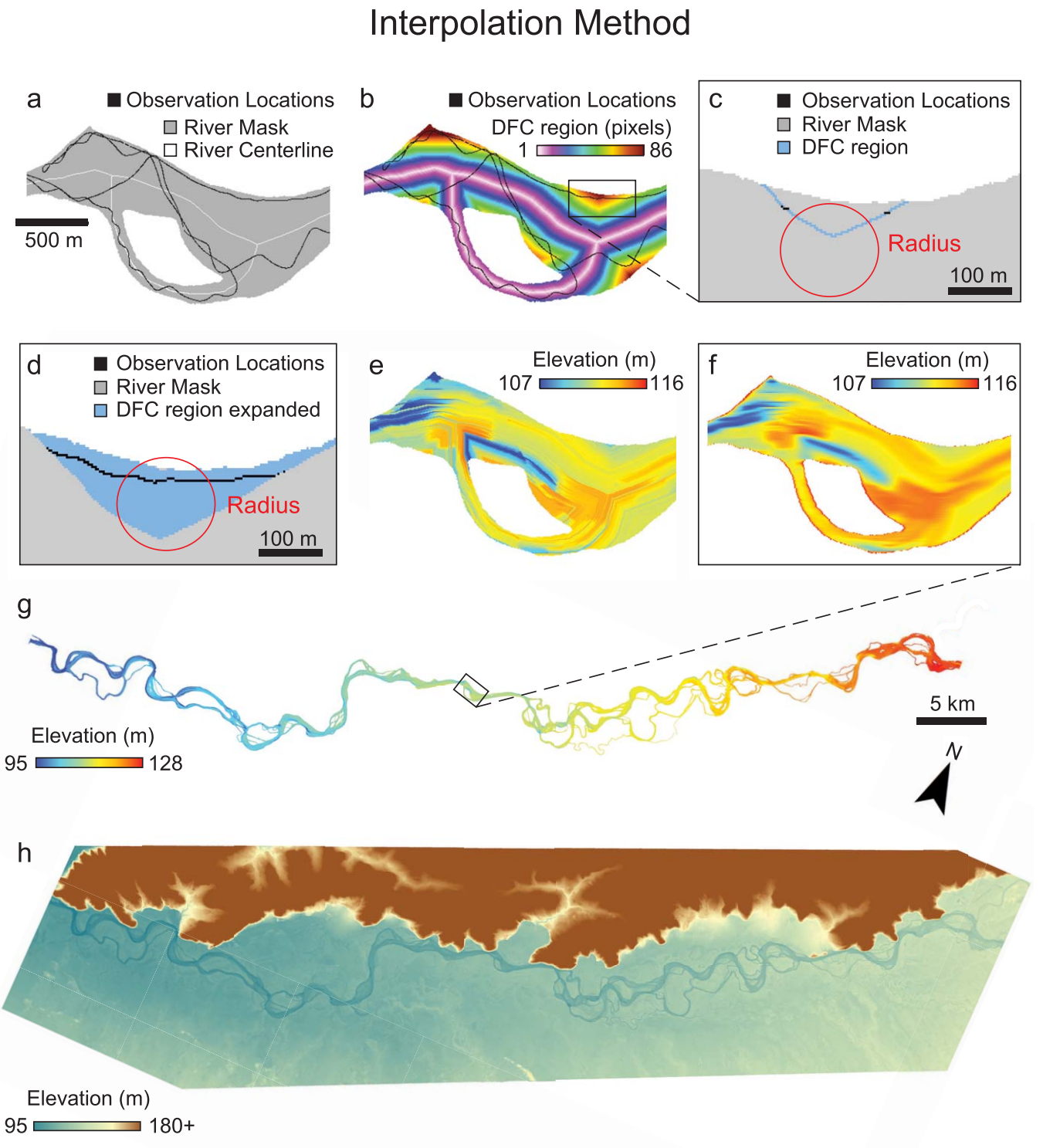

Figure 4. Schematic of the custom interpolation method. (a) Input needed for the interpolation. (b) Distance-from-centerline (DFC) image used to interpolate in the general flow orientation. (c) For each pixel, the DFC region is identified, and all observation points are isolated to those falling within the DFC region and a specified radius. (d) The code expands into adjacent DFC regions to identify a minimum number of observations. (e) Inverse distance weighting (IDW) is performed on the observations. (f) A Gaussian smoothing filter is applied to the entire image. (g) Final interpolated output for the ~90 km river reach. (h) Final seamless DEM of the combined interpolated bathymetry and existing floodplain DEM (Alaska IfSAR).

is repeated for all river pixels. When the entire river is interpolated, we apply a Gaussian smoothing filter to remove high-frequency variability associated with data-sparse areas (Figures 4f and 4g).

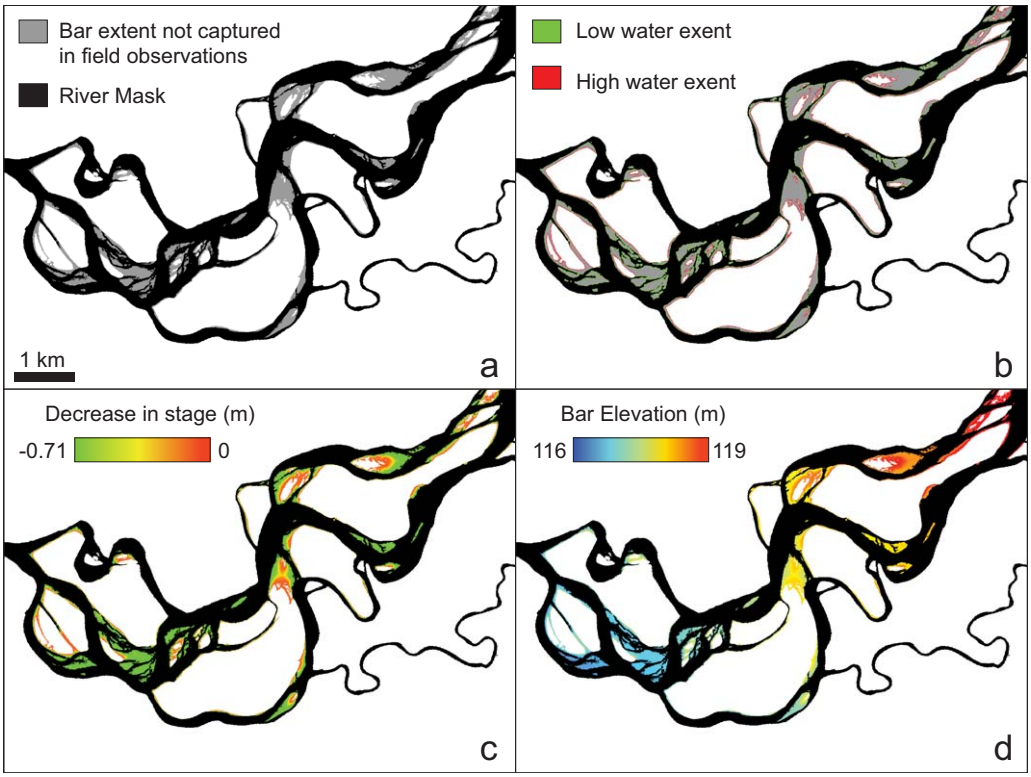

Figure 5. Schematic of the process used to correct submerged bar elevations in the interpolated bathymetry (Figure 4). (a) Submerged bar areas identified using RapidEye imagery at low water levels. (b) Contours of low and high water extents created using the bar areas. High water contours (red) were given a value of zero and low water contours (green) were assigned a negative stage value calculated using USGS gauge records. (c) Interpolated stage values for the identified bar areas. Inverse distance weighting (IDW) was used for interpolation. (d) Converted elevation values. Interpolated stage values were subtracted from linearly interpolated water surface elevation observations collected in the field.

The depth range for the echo sounder is 0.30–75 m (http://www.ohmex.com/sonarmite.html). As a result, our survey includes few observations in very shallow portions of the river reach ($\leq$0.30 m), and interpolated values are likely too deep in these areas. Without additional modifications, diagnostic model runs produce unrealistically low width variations. To diminish this problem, we apply corrections to the interpolation in shallow areas around submerged bars (Figure 5). First, we create a second river mask identifying areas of exposed bars at low summertime flows (1185.4 m^3/s) using RapidEye imagery acquired on 14 August 2012, and we use the river mask from the initial interpolation to define the high-water bar extents at higher flows (1449.3 m^3/s). This comparison allows us to convert stage differences between imagery dates to elevation values using field observations of WSE. Next, we create a bar mask from differences in the two river masks to isolate areas of exposed bars at low water levels (Figure 5a). We use USGS gauge records to calculate stage differences between high and low water levels and to create stage contours that represent high and low bar extents (Figure 5b). To estimate the stage differences between these contours, we use the same IDW formula from the original interpolation (Figure 5c). Finally, we convert the stage differences to elevation changes using the field survey of spatially distributed WSEs (Figure 5d). This correction results in more realistic bar extents in areas that are not captured in the field data. We combine the final bathymetry with the floodplain DEM to create the topographic input for the model simulations (Figure 4h). Over time, the sandbars are likely to shift and change morphology due to the mobility of the Tanana riverbed. However, the timescale of the simulation and the moderate discharges observed in this study make it unlikely that there would be significant changes in the bars that would affect the model outputs. Once the DEM is finalized, we resample the 5 m DEM to 10, 25, 100, and 500 m resolutions using bilinear interpolation in ArcGIS.

We perform a bootstrapping error estimation for the bathymetry by randomly removing 20% of the observational points before implementing the interpolation and using the removed points to calculate RMSE. This bootstrapping method is common in other riverbed interpolation studies [*Osting*, 2004; *Merwade et al.*,

2006; *Merwade*, 2009]. To test the effects of the percentage of points removed, and random sample generation on the calculated errors, we perform a sensitivity analysis on the interpolation. Four different random samples removing 20% of the points are tested, as well as a single random sample removing 1, 5, 10, and 20% of the points. We find the interpolation to be insensitive to the percentage of points and random sampling techniques used with a maximum difference in RMSE of 0.07 m. Final RMSE for the interpolated DEM is 0.890 m. Since the points we use to calculate errors in the bathymetry are extracted from the original depth observations, the estimated error is representative of areas in the bathymetry with higher observational density. In areas where we have limited observations, errors may be much greater than the calculated RMSE and could be a substantial contributor to model errors, especially in the 2-D models where small variations in bathymetry are likely to have larger effects on WSE.

4.4. Model Structures

To test the effects of spatial resolution and dimensionality on model output, we build six different models (Table 1). The fundamental architecture of LISFLOOD-FP consists of a 2-D floodplain component and a 1-D channel component. In our study, discharge volumes throughout the simulations do not reach water levels high enough for overbank flow. Therefore, when referring to 1-D/2-D model structures we are solely referring to channelized flow dimensionalities and do not consider the 2-D floodplain component as part of our model descriptions.

The most detailed model is a 2-D, 10 m resolution model (10 m 2-D) with 9,996,801 grid cells. We also run 2-D simulations at 25 m (25 m 2-D) and 100 m (100 m 2-D) resolutions with 1,600,518 and 99,998 grid cells, respectively. In addition to the 2-D simulations (Figures 1a and 1d), we build a hybrid 1-D/2-D model at 100 m resolution in which the main channel is represented in 2-D and 32 smaller channels are represented as subgrid features in 1-D (100 m SGC) (Figures 1b and 1e). This model contains the same number of grid cells as the 100 m 2-D model but has additional representation of the 32 subgrid channels. Finally, we run two simulations at 500 m resolution, in which a 1-D main channel centerline represents the entire study reach (Figures 1c and 1e) and is treated as a subgrid channel so these models are effectively 1-D with no 2-D channel component. One of the 500 m simulations contains variable bed elevations along the reach (500 m 1-D-VAR), and the other simulation contains a smooth bed slope created using an average water depth value for the entire reach (500 m 1-D-AVG). Both 500 m models have 4010 grid cells.

The models that include subgrid representations require specification of width and bed elevation values for each subgrid channel. We manually assign each subgrid channel in the 100 m SGC model an average width measured from the river mask and an average bed elevation calculated from the surveyed field observations. For each cell along the channel centerlines in the 500 m 1-D models, we assign individual width and bed elevation values. We calculate width values from the 5 m resolution river mask using RivWidth and average the width values at 500 m resolution. For the 500 m 1-D-VAR model, we average bed elevation observations within each grid cell, while for the 500 m 1-D-AVG model we subtract the average water depth value from the observed WSE slope along the study reach.

Table 1. Model Descriptions

Model Acronym	Model Description	Simulation Time (min)
10 m 2-D	2-D flow simulation of the river channels at 10 m resolution	25,992
25 m 2-D	2-D flow simulation of the river channels at 25 m resolution	2,588
100 m 2-D	2-D flow simulation of the river channels at 100 m resolution	19.6
100 m SGC	Hybrid 1-D/2-D model: 2-D flow simulation of the main river channel. 1-D flow simulation of 32 channels with average widths narrower than the model resolution of 100 m using the subgrid solver	9.8
500 m 1-D-VAR	1-D flow simulation of the entire river using the subgrid solver. Bathymetry varies in each grid cell and is estimated by averaging observational depths falling within a channel grid cell	0.2
500 m 1-D-AVG	1-D flow simulation of the entire river using the subgrid solver. Bathymetric slope is estimated from an average depth value calculated from the observations	0.2

5. Model Calibrations and Simulations

The main parameter needed for calibration in each model is the roughness coefficient, in this case Manning's *n*. We calibrate uniform roughness values for the river channel in each model using the spatially distributed observations of WSE and depth collected by boat from 1 July 2013 to 8 July 2013. We choose to use a uniform roughness value because this parameter compensates for many factors affecting the simulated flow, including the hydraulic resistance from bed formations, model dimensionality, grid resolution, model process representation, and errors in the boundary conditions [*Bates et al*., 2013]. In a river as large as the Tanana, errors in the inflow boundary conditions and bathymetry are likely to dominate model errors compared to small-scale variations in sediment composition. Additionally, the complex planform makes it difficult to identify obvious zones of different roughness values within the study reach. For the floodplain roughness, we assign a standard uniform value of 0.06. We do not calibrate the floodplain roughness value since there is no overbank flow occurring in our simulations.

Before running the calibrations, we correct the WSE variations between dates of the boat observations to 1 July using the temporally varying observations of WSE recorded by the water loggers. We test roughness values between 0.008 and 0.06 completing a total of 55 calibration runs per model. Model calibrations begin on 29 June 2013 and end on 2 July 2013. The first day of the simulations is model spin-up time. Once the calibrations are complete, we run 63-day dynamic simulations for each model from 29 June 2013 to 31 August 2013 using the optimal roughness value for each model. The simulations span the entire period measured by the two water loggers. Final computation times per simulation range from 0.2 min to 18 days on a 2.40 GHz Intel Xeon 6 core processor with 40 GB of RAM (Table 1). The LISFLOOD-FP code is parallelized to use all cores available on a machine.

6. Model Validation

We evaluate each model's ability to simulate inundation extent, temporally varying WSE, and spatial patterns in WSE and depth. To validate inundation extent, we compare model spatial outputs to a 5 m resolution river mask created with RapidEye imagery from 1 August 2013. The maximum variation in discharge at the Nenana gauge station on 1 August is 48 m^3/s. This range in flow comprises 2.5% of the average discharge of 1895 m^3/s on that date and is unlikely to result in changes to the channel extent within the observed river mask. We resample model outputs to 5 m resolution for direct comparison to the observed river mask and classify both the observed and modeled outputs as inundated or dry pixels. Errors of commission are considered areas where the model produces inundated pixels and the observations show dry pixels, while errors of omission are areas where the model produces dry pixels and the observations show inundated pixels. We count inundated pixels in both the models and observations as correctly modeled areas. Lastly, we calculate a measure of fit statistic (also known as the Critical Success Index (CSI) in the meteorological forecast literature) to further assess the models' capabilities for simulating river inundation extent:

$$Fit\ (\%) = \frac{IA_{obs} \cap IA_{mod}}{IA_{obs} \cap IA_{mod}} \times 100. \tag{8}$$

The CSI compares the observed inundation (IA_{obs}) to the modeled inundation (IA_{mod}) and penalizes model over and underpredictions [*Bates et al*., 2010; *Sampson et al*., 2015], but is not biased by the large and easy to predict areas observed and correctly simulated as dry.

To estimate spatial errors in model outputs, we use the 20% of survey points we removed before the bathymetric interpolation to calculate RMSE, mean bias, and absolute errors between model outputs and spatially distributed observations of WSE and depth. Additionally, we analyze WSE errors along 1-D river profiles. We create the 1-D profiles by deriving a centerline vector along the main channel of the river using RivWidth and compare the in situ WSE observations along the centerline to model-derived WSE. Since the spatial observations were collected from 1 July 2013 to 8 July 2013, we average the model spatial outputs from this timespan before comparing them to the observations. We then calculate RMSE and Nash-Sutcliffe Efficiency (NS) values [*McCuen et al*., 2006] for the river profile and for each of the subreaches. Finally, we validate temporal fluctuations in modeled WSE by calculating NS values against observations at the two water logger locations. To assess the effects of discharge uncertainty on model outputs, we perform a sensitivity

analysis on the 25 m 2-D model by running simulations with ±10% and ± 20% differences in the upstream discharge.

7. Results

Model errors in spatially distributed WSE significantly increase and the CSI substantially worsens as model resolution coarsens and dimensionality decreases. The 10 and 25 m 2-D models are best at capturing spatially distributed WSE and inundation extent within the main channel and subchannels (Figure 6). Absolute errors in spatially distributed WSE are lowest and evenly spread along the reach in the 25 m 2-D and 10 m 2-D models (Figure 6b). The primary area of overpredicted WSEs in these simulations occurs where the anabranching subreach converges into the single channel subreach. Improved RMSE from the 25 m to the 10 m 2-D model is minimal for spatially distributed WSE but more substantial for depths, with a ∼10 cm improvement in RMSE (Table 2). Along the observed profile, both models show similar patterns in WSE variations, but the 10 m 2-D model slightly outperforms the 25 m 2-D model at the downstream end of the study reach (Figures 7a and 7b and Table 3). The CSI for inundated area is strongest in the 10 m 2-D (90.3%) and 25 m 2-D (88.5%) models (Table 4). Both the 25 and 10 m model resolutions are fine enough to capture proper channel morphology and subchannel connectivity in 2-D (Figure 6a). Primary errors of commission for the 10 and 25 m 2-D models result from bathymetric uncertainties in areas with little observational data, especially around bar formations. These shallow, erroneously inundated areas affect the CSI but do not substantially affect simulation of discharge. Roughness coefficients in the 10 m 2-D and 25 m 2-D model simulations are most consistent with the literature (Table 2). Roughness values can range from 0.026 to 0.08 in channels with morphological characteristics and sediment types similar to the Tanana River [*Chow*, 1959; *Arcement and Schneider*, 1989; *Toniolo*, 2013].

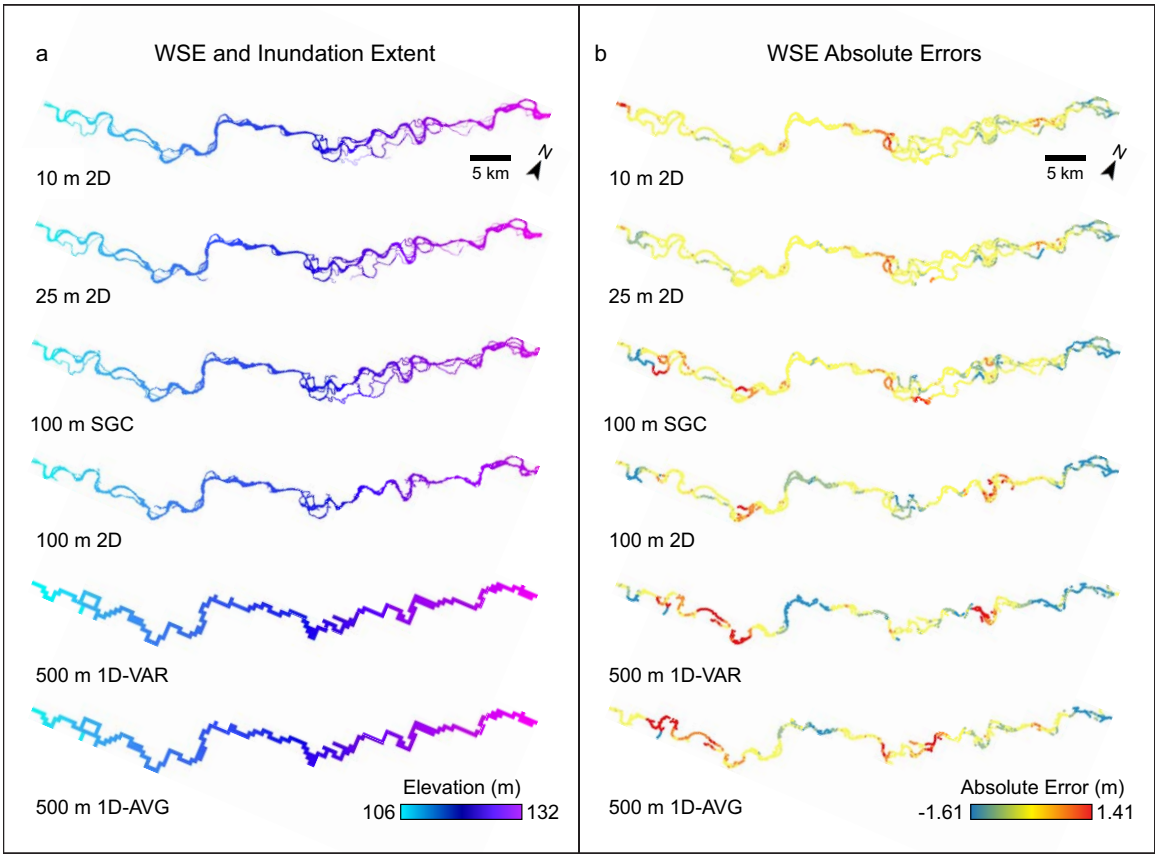

Figure 6. Spatial output of (a) WSE and inundation extent and (b) absolute errors between the modeled and observed WSE on 1 July 2013.

Table 2. Error Statistics for Spatial and Temporal Model Outputs

Model	RMSE WSE (m)	RMSE Depth (m)	Bias WSE (m)	Bias Depth (m)	NSE Upstream	NSE Upstream (Bias)	NSE Downstream	NSE Downstream (Bias)	Roughness Coefficient
10 m 2-D	0.226	0.712	−0.011	−0.075	0.341	0.945	0.844	0.881	0.023
25 m 2-D	0.259	0.794	−0.014	−0.019	0.747	0.943	0.742	0.859	0.021
100 m SGC	0.318	1.51	−0.053	0.241	0.783	0.873	0.317	0.758	0.014
100 m 2-D	0.379	1.62	0.0019	0.301	−2.258	0.903	0.633	0.756	0.011
500 m 1-D-VAR	0.564	2.54	0.070	0.646	−5.199	0.709	−5.539	0.734	0.010
500 m 1-D-AVG	0.352	1.88	0.028	0.321	−0.634	0.977	0.495	0.970	0.017

More prominent patterns in the errors of spatially distributed WSE become apparent in the 100 m model simulations (Figure 6b). The 100 m SGC model outperforms the 100 m 2-D model by preserving channel connectivity with the inclusion of the 1-D subgrid channels, which increases channel capacity and reduces overall errors in the anabranching subreach, in particular. In contrast, the 100 m 2-D model tends to overpredict WSEs in the anabranching subreach. These overpredictions are likely a result of a decrease in

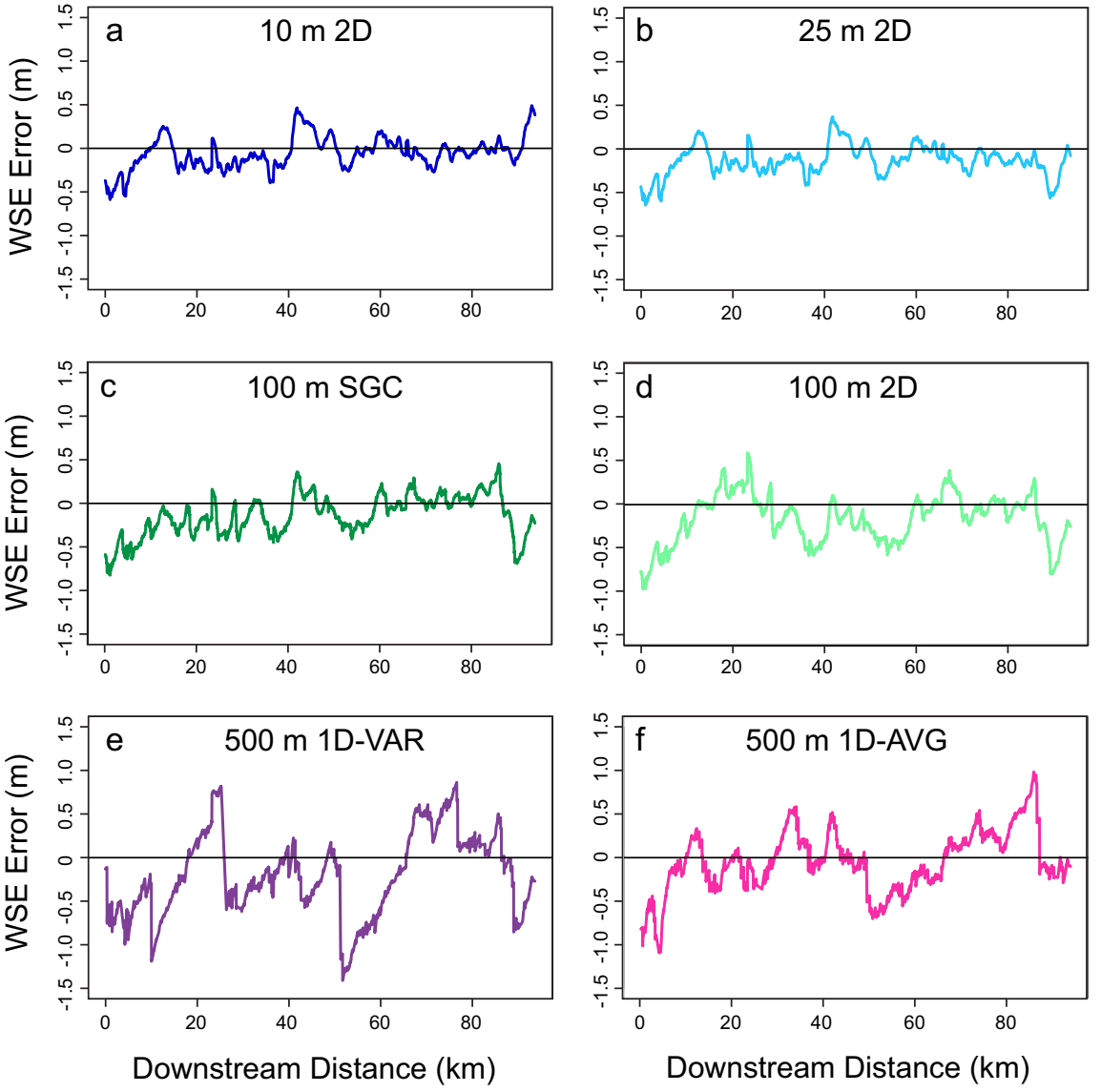

Figure 7. Plots of modeled WSE errors along the main channel profile.

Table 3. Error Statistics of WSE Along the Main Channel Profile[a]

	Entire Reach		Upstream		Anabranching		Single		Downstream	
Model	RMSE	NS	RMSE	NS	RMSE	NS	RMSE	NS	RMSE	NS
10 m 2-D	0.194	0.9990	0.282	0.9595	0.207	0.9889	0.160	0.9708	0.137	0.9952
25 m 2-D	0.217	0.9988	0.309	0.9514	0.207	0.9889	0.174	0.9652	0.187	0.9911
100 m SGC	0.276	0.998	0.437	0.9029	0.256	0.983	0.194	0.9571	0.216	0.9881
100 m 2-D	0.322	0.9973	0.475	0.8854	0.285	0.9789	0.329	0.8761	0.245	0.9846
500 m 1-D-VAR	0.517	0.993	0.627	0.8073	0.359	0.9672	0.745	0.3664	0.415	0.956
500 m 1-D-AVG	0.351	0.9968	0.452	0.8996	0.259	0.9829	0.396	0.8210	0.332	0.9719

[a]Headings coincide with the subreaches defined in Figure 3.

channel capacity from the loss of the bifurcating channels at the coarser resolution (Figures 6b, 7c, and 7d). Additionally, incorporating the channel connectivity using the subgrid channels decreases RMSE by ~16% for spatially distributed WSE and ~7% for depths in the 100 m SGC model compared to the 100 m 2-D model (Table 2). The coarser resolution of the 100 m models approaches the limit for representing the Tanana River morphology in 2-D by averaging out the small anabranching channels whilst preserving the larger main channels. Therefore, the CSIs for inundation extent in the 100 m models are lower than the 10 and 25 m 2-D models at 72.6% for the 100 m SGC model and 72.2% for the 100 m 2-D model (Table 4).

The anabranching channel network is not simulated at 500 m resolution, and distinct alternating patterns emerge in the absolute errors of spatially distributed WSE (Figure 6). Absolute errors in both 500 m models alternate between underpredicting WSE by as much as 1.61 m and overpredicting WSE by 1.41 m (Figures 7e and 7f). These alternating patterns result in low mean biases for spatially distributed WSE in the 500 m models even though the models do not accurately represent the spatial dynamics. The 500 m 1-D-AVG model shows 38% improvement in RMSE for spatial patterns of WSE compared to the 500 m 1-D-VAR model, and a slightly better RMSE compared to the 100 m 2-D model, though the alternating patterns in absolute errors are still present along the reach (Table 2 and Figures 6b and 7f). In addition to high errors in spatially distributed WSE, the 500 m models poorly predict inundated area, with CSIs around 41% (Table 4). These low CSIs are due to large overpredictions in inundated area as a result of the coarse grid size, which averages the main channel and subchannels into a single raster cell (Figure 6a). Roughness coefficients decrease as model process representation simplifies from the 2-D models to the 500 m 1-D-VAR model, with the exception of the 500 m 1-D-AVG model, which displays a roughness value higher than both the 100 m models and 500 m 1-D-VAR model (Table 2). The increase in model roughness value in the 500 m 1-D-AVG model is likely a result of its smoother bathymetric slope. The variations in the bed topography in the 100 and 500 m 1-D-VAR models have higher friction effects compared to the smooth bed slope of the 500 m 1-D-AVG model. This increase in friction from the bed topography in the 100 and 500 m 1-D-VAR models requires a lower roughness coefficient compared to the 500 m 1-D-AVG model to balance the higher bathymetric roughness.

Temporal variations in WSE from all models at both water logger locations show good agreement with observations in predicting WSE fluctuations, but large biases from the observed WSEs occur depending on the model structure. Time series of WSE outputs and errors for each model are shown in Figure 8, and associated NS values are in Table 2. Upstream water logger results show consistent overpredictions in the 500 m 1-D-VAR and 100 m 2-D models, and consistent underpredictions in the 500 m 1-D-AVG model. These poor model performances are reflected in the NS values, which are well below zero. The large deviations are likely caused by spatial biases stemming from bathymetric uncertainties and reduced channel connectivity that result in overpredictions in WSE levels at the upstream water logger location in the 500 m 1-D-VAR and 100 m 2-D models. By comparison, the 100 m SGC and 25 m 2-D models produce more accurate

Table 4. Percentage Statistics and Measure of Fit for Modeled River Inundation Extent

Model	Correctly Modeled Area (%)	Errors of Commission (%)	Errors of Omission (%)	Critical Success Index (%)
10 m 2-D	96.42	6.69	3.58	90.37
25 m 2-D	95.41	7.80	4.59	88.51
100 m SGC	88.66	22.17	11.34	72.57
100 m 2-D	80.04	10.84	19.96	72.21
500 m 1-D-VAR	70.51	72.74	29.49	40.82
500 m 1-D-AVG	71.20	73.17	28.80	41.12

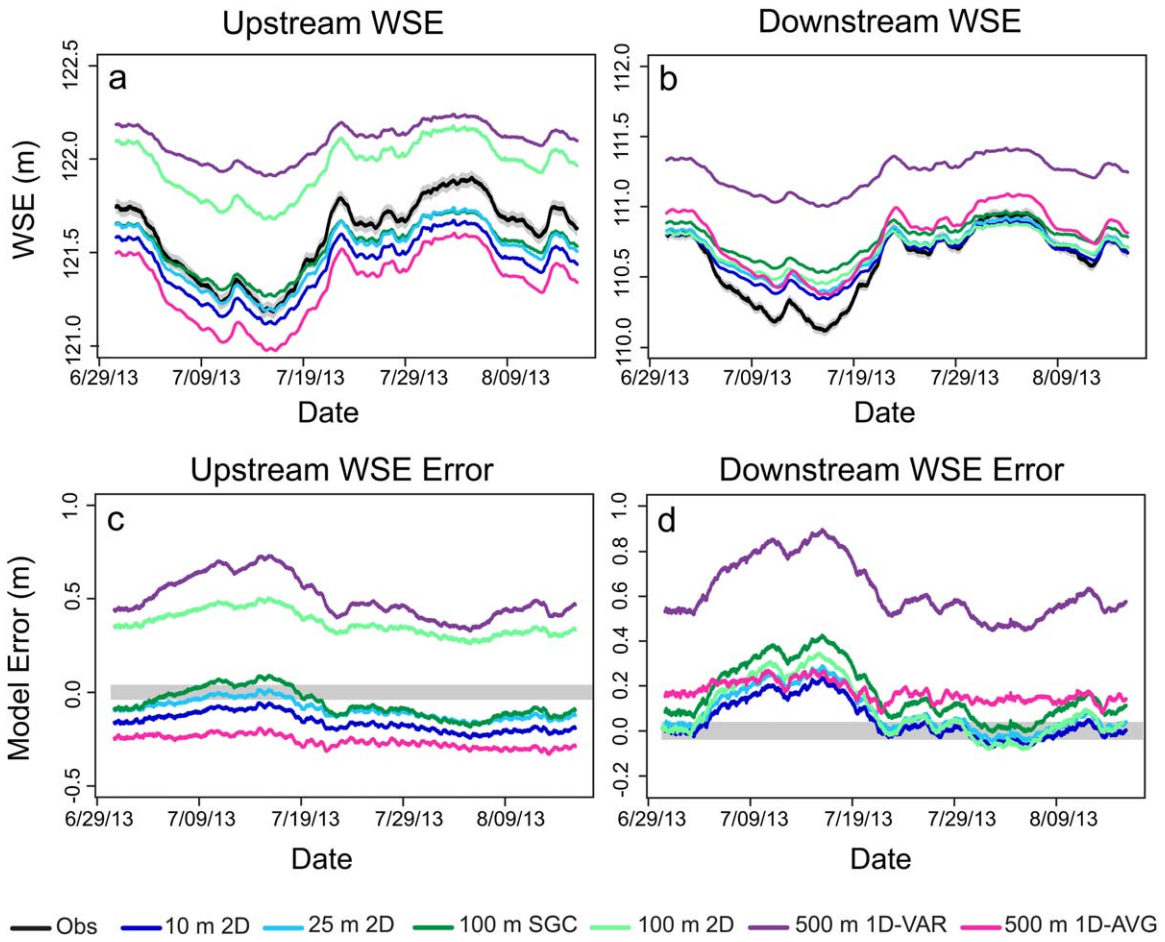

Figure 8. Temporal variations and absolute errors in modeled WSE. The (a, c) upstream and (b, d) downstream water logger locations are ~23 and ~70 km downstream of Fairbanks, respectively (Figure 2). Figures 8a and 8b display the modeled WSEs versus observations over time, while Figure 8c and 8d display model WSE errors. Gray shaded areas represent observational errors.

temporal dynamics with NS values of 0.783 and 0.747, respectively. The 25 m 2-D model follows the observations most closely during low water intervals, while the 10 m 2-D model underpredicts WSE, reducing the upstream NS value to 0.341. During high stage intervals the 100 m SGC, 25 m 2-D, and 10 m 2-D models all underpredict WSE (Figures 8a and 8c).

WSE dynamics at the downstream water logger show reverse patterns for most of the models. The 500 m 1-D-VAR model continues to overpredict WSE by about half a meter. However, the 500 m 1-D-AVG model switches from consistently underpredicting WSE at the upstream location to being much closer to the observations at the downstream location with an improved NS value of 0.495. The other four models tend to overpredict WSE at low water intervals and come closer to the observations at high water intervals (Figures 8b and 8d). Performances between the 100 m SGC and 100 m 2-D models switch at the downstream location with the 100 m SGC model's NS value dropping to 0.317 and the 100 m 2-D model's NS value increasing to 0.633. The 25 m 2-D model performance stays consistent downstream with an NS value of 0.742, while the 10 m 2-D model performance improves with an NS value of 0.844 (Table 2).

To determine the effects of spatial errors on temporal outputs, we subtracted the mean bias for each model at the upstream and downstream water logger locations and recalculated NS values (Table 2). Variances in model performances decrease and NS values for all models greatly increase when subtracting out the biases. However, model performances gradually diminish as the resolution coarsens and dimensionality decreases. The one exception is the 500 m 1-D-AVG model, which shows the best and most consistent performance after subtracting out the mean bias with NS values of 0.977 upstream and 0.970 downstream.

Observational errors for the water loggers are small at ±0.04 m and do not significantly affect the temporal results. However, errors in discharge associated with the model boundary conditions could have a substantial effect on model outputs. Results of the sensitivity analysis show a 14–62% increase in spatial RMSE for a ±10% to ±20% change in discharge. Additionally, depending on spatial location of the observations, NS values for temporal model outputs drop well below zero for a ±20% change in discharge and display a large range in NS values of −0.005 to 0.873 for a ±10% change in discharge.

8. Discussion and Conclusion

This study is the first to test a simple, raster-based model's ability to simulate 2-D, in-channel flows along a ∼100 km reach of a multichannel river. We find that given proper parameterization and input information, raster-based models like LISFLOOD-FP can produce accurate 2-D simulations of spatial patterns in WSE and inundation extent. Both the 10 m 2-D and 25 m 2-D models produce RMSE values less than 0.26 m for spatially distributed WSE and have a CSI for inundation extent of at least 89% (Tables 2 and 4). These CSIs approach the maximum performance achieved when using hydraulic models, even when built using detailed LiDAR data [*Bates et al*., 2006; *Neal et al*., 2009]. RMSE for the spatially distributed observations of WSE and depth are 0.162 and 0.267 m, suggesting that observational error likely accounts for a significant portion of the model errors, in addition to discharge uncertainties and model structural errors.

Bathymetric uncertainties likely exert a dominant control on patterns in spatially distributed WSE errors in both the 10 and 25 m 2-D models. Certain areas of the Tanana were inaccessible by boat due to shallow subchannels, log jams, or submerged bars. This inaccessibility results in little to no observational data in these areas and larger uncertainties in the interpolated bathymetry. Based on the interpolation results, errors in the bathymetry that are father away from our observations could be greater than 0.890 m. These bathymetric uncertainties likely manifest as higher localized errors in modeled WSE in the small subchannels and in areas of significant change in planform along the reach (Figure 6b). For example, the 2-D models tend to overpredict WSE in areas where multiple channels collapse into a single channel. The larger WSE errors in areas of morphological change could also be a result of model structural errors from the exclusion of advection in the momentum equation. Additionally, the uniform roughness coefficient used here likely fails to capture spatial variations present in an environment as complex as the Tanana. It is possible that errors occurring at significant morphological transitions, as well as some of the errors caused by bathymetric uncertainties, could be lowered using spatially varying roughness coefficients along the reach. More research is needed to investigate the controlling factors on roughness values in multichannel rivers at reach scales ≥100 km.

Analysis of temporal dynamics in WSE highlights larger differences between the 10 and 25 m 2-D models. At the downstream water logger location, both models produce reasonable NS values, though they slightly overpredict WSE at low water intervals. However, at the upstream water logger location, the 10 m 2-D model's performance drops substantially in comparison to the 25 m 2-D model due to consistent underpredictions of WSE throughout the span of the simulation (Table 2 and Figure 8). Differences in temporal WSE variations between the 10 and 25 m 2-D models are likely caused by spatial biases due to bathymetric uncertainties and differences in channel connectivity due to model resolution. The finer spatial resolution of the 10 m model allows better connectivity in some of the anabranching subchannels compared to the 25 m model (Figure 6a). This increase in channel connectivity, combined with bathymetric errors, likely distributes more flow to the subchannels upstream of the water logger location, which decreases the flow and lowers WSE in the main channel where the observations are recorded. The effect of spatial biases in the temporal results is demonstrated when subtracting out the mean bias in the model outputs. Without spatial biases, the 10 m 2-D and 25 m 2-D models have negligible differences in NS values at the upstream and downstream water logger locations (Table 2). In the future, access to a larger observational network of water loggers measuring temporally varying WSE would provide more insight into model limitations and spatiotemporal controls on WSE throughout the study reach.

Despite limitations, results from the 2-D model analysis demonstrate the practical application of a simple, raster-based model in simulating 2-D channel hydraulics in multichannel river environments across 100 km reach scales. These efficient 2-D models are important for future analysis of new remote sensing observations from sensors such as the Surface Water and Ocean Topography Mission (SWOT), which is scheduled to

launch in 2021 [*Biancamaria et al*., 2016]. SWOT aims to record spatially continuous, 2-D observations of WSE and slope for the world's rivers 50–100 m in width and greater (http://swot.jpl.nasa.gov/). However, it is not clear how effectively SWOT will observe multichannel systems. Fine-resolution, 2-D model outputs of in-channel WSE are needed for prelaunch simulation and post-launch data assimilation of SWOT observations [*Durand et al*., 2008; *Biancamaria et al*., 2011, 2016; *Bates et al*., 2014]. Additionally, scientists and managers can use efficient 2-D models like those tested here to help identify areas that are vulnerable to flooding in these complex environments [*Surian*, 2015].

Comparisons between the detailed 2-D models and models of lower dimensionality and coarser resolution reveal that bathymetry is a predominant control on WSE in the finer resolution 2-D models, while simplifications to the multichannel network exert a larger control on WSE in the coarser resolution, 1-D models. The 10 and 25 m 2-D models provide the highest level of process representation along the study reach. In these models, spatial and temporal errors in WSE are primarily influenced by spatial biases from bathymetric errors (Figures 6 and 8). As model resolution coarsens to 100 m, a combination of bathymetric uncertainties and improper channel connectivity dominate model errors. Many of the small subchannels are lost in the anabranching subreach due to the coarser grid size in the 100 m 2-D model. As a result, larger overpredictions in WSE occur in this subreach due to a decrease in channel capacity. Representing the smaller subchannels using subgrid representations, as in the 100 m SGC model, results in more evenly spaced WSE errors and a ~16% decrease in RMSE. Additionally, including channel connectivity using the subgrid channels in the 100 m SGC model improves temporal WSE dynamics compared to the 100 m 2-D model (Table 2 and Figure 8).

The elimination of the anabranching morphology is the prominent factor influencing spatial and temporal hydraulics in the 500 m 1-D models when compared to the finer resolution models. This is demonstrated through the differing bathymetric conditions in the 500 m models. The 500 m 1-D-VAR model's bed slope contains larger variations along the reach compared to the smooth bed slope in the 500 m 1-D-AVG model. While the smoother bed slope of the 500 m 1-D-AVG model reduces the average spatial error in WSE compared to the 500 m 1-D-VAR model, both models produce notable alternating patterns in spatially distributed WSE errors (Figure 6b and Figure 7). These alternating errors are likely a result of unrealistic decreases or increases in channel capacity as the anabranching channels are averaged together at the coarser resolution and represented as single effective width values in the 1-D model structure. Additionally, the general drop in roughness coefficients from the 2-D models to the 1-D models reflects the effects of simplifying the multichannel network. The decrease in roughness with coarser model resolution is likely due to the spatial averaging of bathymetry across multiple channels, which reduces the overall channel capacity and requires a lower friction value to convey the same discharge dynamics along the study reach. As a result, large biases emerge in the models' temporal dynamics that indicate the 500 m model performances are no better (or even worse) than the mean of the observations in many locations and are likely to misrepresent hydraulics in multichannel rivers like the Tanana.

Various 1-D solvers, like the one in this study, are the primary hydraulic routing methods currently used in regional to global-scale models [*Yamazaki et al*., 2011; *Schumann et al*., 2014b,; *Sampson et al*., 2015]. The results of this study demonstrate the importance of channel bifurcations and convergences in accurately simulating WSE in multichannel systems, which are not accounted for in regional and global models. As a result, these 1-D solvers can produce significant model errors in spatial and temporal WSE dynamics in multichannel rivers due to the neglect of anabranching channels. Large errors in WSE along river reaches can result in improper flood predictions and slope estimates that could lead to incorrect discharge estimates in data sparse regions [*Durand et al*., 2008].

Future development of regional to global-scale models requires better observational data of WSE and bathymetry to calibrate and validate channel hydraulics in multichannel river environments. The SWOT mission plans to substantially improve spatial coverage of river WSE and slope observations at regular temporal intervals, which will help to improve models through data assimilation and improved boundary conditions [*Bates et al*., 2014; *Biancamaria et al*., 2016]. In the meantime, regional and global-scale models of large multichannel rivers can be improved by using downscaling techniques or subgrid channel schemes that allow for better representation of anabranching channel networks, rather than lumping the channel conveyance into a single effective centerline [*Neal et al*., 2012a; *Schumann et al*., 2014b; *Sampson et al*., 2015]. If results

on the Tanana hold true for other rivers, then models such as the 100 m SGC model presented here would come close to matching the accuracy of 2-D simulations without the required computational burden.

Acknowledgments
This work was supported by NASA Terrestrial Hydrology Program grant NNX13AD05G managed by Jared Entin. Field locations and observations of water surface elevation were based on equipment services provided by the UNAVCO Facility with support from the National Science Foundation (NSF) and National Aeronautics and Space Administration (NASA) under NSF Cooperative Agreement EAR-0735156. We want to thank our boat driver Sam Demientieff for his navigational expertise on the Tanana River, which allowed for safe and timely data collection. An additional thanks goes to the two anonymous reviewers and Associate Editor who provided comments that helped improve the quality of the manuscript. LISFLOOD-FP is available for noncommercial research purposes by contacting Paul Bates at the University of Bristol (paul.bates@bristol.ac.uk). RapidEye imagery is available to purchase at (http://www.satimagingcorp.com/satellite-sensors/other-satellite-sensors/rapideye/). The custom interpolation code and any observational data used in this study are available upon request to Elizabeth H. Altenau (ealtenau@unc.edu).

References

Allen, G. H., and T. M. Pavelsky (2015), Patterns of river width and surface area newly revealed by the satellite-derived North American River Width (NARWidth) dataset, *Geophys. Res. Lett.*, *42*, 395–402, doi:10.1002/2014GL062764.

Arcement, G. J., and V. R. Schneider (1989), Guide for selecting Manning's roughness coefficients for natural channels and flood plains United States, *U.S. Geol. Surv. Water Supply Pap.*, *2339*, 1–38.

Bates, P. D., and A. P. J. De Roo (2000), A simple raster-based model for flood inundation simulation, *J. Hydrol.*, *236*(1–2), 54–77, doi:10.1016/S0022-1694(00)00278-X.

Bates, P. D., M. S. Horritt, N. M. Hunter, D. Mason, and D. Cobby (2005), Numerical modelling of floodplain flow, in *Computational Fluid Dynamics: Applications in Environmental Hydraulics*, edited by P. D. Bates, S. N. Lane, and R. I. Ferguson, pp. 271–304, John Wiley, Chichester, U. K.

Bates, P. D., M. D. Wilson, M. S. Horritt, D. C. Mason, N. Holden, and A. Currie (2006), Reach scale floodplain inundation dynamics observed using airborne synthetic aperture radar imagery: Data analysis and modelling, *J. Hydrol.*, *328*(1), 306–318, doi:10.1016/j.jhydrol.2005.12.028.

Bates, P. D., M. S. Horritt, and T. J. Fewtrell (2010), A simple inertial formulation of the shallow water equations for efficient two-dimensional flood inundation modelling, *J. Hydrol.*, *387*(1), 33–45, doi:10.1016/j.jhydrol.2010.03.027.

Bates, P. D., F. Pappenberger, and R. J. Romanowicz (2013), Uncertainty in flood inundation modelling, in *Applied Uncertainty Analysis for Flood Risk Management*, edited by K. Beven and J. Hall, pp. 232–269, Imperial College Press, Singapore.

Bates, P. D., J. C. Neal, D. Alsdorf, and G. J. P. Schumann (2014), Observing global surface water flood dynamics, *Surv. Geophys.*, *35*(3), 839–852, doi:10.1007/s10712-013-9269-4.

Beighley, R. E., K. G. Eggert, T. Dunne, V. Gummadi, and K. L. Verdin (2009), Simulating hydrologic and hydraulic processes throughout the Amazon River Basin, *Hydrol. Processes*, *23*(8), 1221–1235.

Biancamaria, S., M. Durand, K. M. Andreadis, P. D. Bates, A. Boone, N. M. Mognard, E. Rodríguez, D. E. Alsdorf, D. P. Lettenmaier, and E. A. Clark (2011), Assimilation of virtual wide swath altimetry to improve Arctic river modeling, *Remote Sens. Environ.*, *115*(2), 373–381, doi:10.1016/j.rse.2010.09.008.

Biancamaria, S., D. P. Lettenmaier, and T. M. Pavelsky (2016), The SWOT mission and its capabilities for land hydrology, *Surv. Geophys.*, *37*(2), 307–337, doi:10.1007/s10712-015-9346-y.

Bierkens, M. F. P., et al. (2015), Hyper-resolution global hydrological modelling: What is next?: Everywhere and locally relevant, *Hydrol. Processes*, *29*(2), 310–320, doi:10.1002/hyp.10391.

Brabets, T. P., B. Wang, and R. H. Meade (2000), Environmental and hydrologic overview of the Yukon River Basin, Alaska and Canada, *U.S. Geol. Surv. Water Resour. Invest. Rep.*, *99-4204*, 1–106.

Bradbrook, K. F., S. N. Lane, S. G. Waller, and P. D. Bates (2004), Two dimensional diffusion wave modelling of flood inundation using a simplified channel representation, *Int. J. River Basin Manage.*, *2*(3), 211–223, doi:10.1080/15715124.2004.9635233.

Bridge, J. S. (1993), The interaction between channel geometry, water flow, sediment transport and deposition in braided rivers, *Geol. Soc. Spec. Publ.*, *75*(1), 13–71, doi:10.1144/GSL.SP.1993.075.01.02.

Chow, V. T. (1959), *Open-Channel Hydraulics*, 680 pp., McGraw-Hill, New York.

Cloke, H. L., and F. Pappenberger (2009), Ensemble flood forecasting: A review, *J. Hydrol.*, *375*(3), 613–626, doi:10.1016/j.jhydrol.2009.06.005.

Courant, R., K. Friedrichs, and H. Lewy (1928), Partial differential equations of mathematical physics, *Math. Ann.*, *100*, 32–74.

Cunge, J. A., F. M. Holly, and A. Verwey (1980), *Practical Aspects of Computational River Hydraulics*, 420 pp., Pitman, London.

de Almeida, G. A. M., P. D. Bates, J. Freer, and M. Souvignet (2012), Improving the stability of a simple formulation of the shallow water equations for 2-D flood modeling, *Water Resour. Res.*, *48*, W05528, doi:10.1029/2011WR011570.

de Almeida, G. A. M., and P. D. Bates (2013), Applicability of the local inertial approximation of the shallow water equations to flood modeling, *Water Resour. Res.*, *49*, 4833–4844, doi:10.1002/wrcr.20366.

Di Baldassarre, G., and A. Montanari (2009), Uncertainty in river discharge observations: A quantitative analysis, *Hydrol. Earth Syst. Sci.*, *13*(6), 193–921, doi:10.5194/hessd-6-39-2009.

Dornblaser, M. M., and R. G. Striegl (2009), Suspended sediment and carbonate transport in the Yukon River Basin, Alaska: Fluxes and potential future responses to climate change, *Water Resour. Res.*, *45*, W06411, doi:10.1029/2008WR007546.

Durand, M., K. M. Andreadis, D. E. Alsdorf, D. P. Lettenmaier, D. Moller, and M. Wilson (2008), Estimation of bathymetric depth and slope from data assimilation of swath altimetry into a hydrodynamic model, *Geophys. Res. Lett.*, *35*, L20401, doi:10.1029/2008GL034150.

Goff, J. A., and S. Nordfjord (2004), Interpolation of fluvial morphology using channel-oriented coordinate transformation: A case study from the New Jersey Shelf, *Math. Geol.*, *36*(6), 643–658, doi:10.1023/B:MATG.0000039539.84158.cd.

Harmel, R. D., R. J. Cooper, R. M. Slade, R. L. Haney, and J. G. Arnold (2006), Cumulative uncertainty in measured streamflow and water quality data for small watersheds, *Trans. ASABE*, *49*(3), 689–701, doi:10.13031/2013.20488.

Horritt, M. S., and P. D. Bates (2001), Effects of spatial resolution on a raster based model of flood flow, *J. Hydrol.*, *253*(1), 239–249, doi:10.1016/S0022-1694(01)00490-5.

Horritt, M. S., and P. D. Bates (2002), Evaluation of 1D and 2D numerical models for predicting river flood inundation, *J. Hydrol.*, *268*(1), 87–99, doi:10.1016/S0022-1694(02)00121-X.

Horritt, M. S., P. D. Bates, and M. J. Mattinson (2006), Effects of mesh resolution and topographic representation in 2D finite volume models of shallow water fluvial flow, *J. Hydrol.*, *329*(1), 306–314, doi:10.1016/j.jhydrol.2006.02.016.

Hunter, N. M., P. D. Bates, M. S. Horritt, and M. D. Wilson (2007), Simple spatially-distributed models for predicting flood inundation: A review, *Geomorphology*, *90*(3), 208–225, doi:10.1016/j.geomorph.2006.10.021.

Javernick, L., D. M. Hicks, R. Measures, B. Caruso, and J. Brasington (2016), Numerical modelling of braided rivers with structure-from-motion-derived terrain models, *River Res. Appl.*, *32*(5), 1071–1081, doi:10.1002/rra.2918.

Lane, S. N., and K. S. Richards (1998), High resolution, two-dimensional spatial modelling of flow processes in a multi-thread channel, *Hydrol. Processes*, *12*(8), 1279–1298, doi:10.1002/(SICI)1099-1085(19980630)12:8<1279::AID-HYP615>3.0.CO;2-E.

Lane, S. N., K. F. Bradbrook, K. S. Richards, P. S. Biron, and A. G. Roy (1999), The application of computational fluid dynamics to natural river channels: Three-dimensional versus two-dimensional approaches, *Geomorphology*, *29*(1), 1–20, doi:10.1016/S0169-555X(99)00003-3.

Latrubesse, E. M. (2008). Patterns of anabranching channels: The ultimate end-member adjustment of mega rivers, *Geomorphology*, *101*(1), 130–145, doi:10.1016/j.geomorph.2008.05.035.
Legleiter, C. J., and P. C. Kyriakidis (2006), Forward and inverse transformations between Cartesian and channel-fitted coordinate systems for meandering rivers, *Math. Geol.*, *38*(8), 927–958, doi:10.1007/s11004-006-9056-6.
Legleiter, C. J., and P. C. Kyriakidis (2008), Spatial prediction of river channel topography by kriging, *Earth Surf. Processes Landforms*, *33*(6), 841–867.
McCuen, R. H., Z. Knight, and A. G. Cutter (2006), Evaluation of the Nash–Sutcliffe efficiency index, *J. Hydrol. Eng.*, *11*(6), 597–602, doi: 10.1061/(ASCE)1084-0699(2006)11:6(597).
McFeeters, S. K. (1996), The use of the Normalized Difference Water Index (NDWI) in the delineation of open water features, *Int. J. Remote Sens.*, *17*(7), 1425–1432, doi:10.1080/01431169608948714.
Merwade, V. M., D. R. Maidment, and B. R. Hodges (2005), Geospatial representation of river channels, *J. Hydrol. Eng.*, *10*(3), 243–251, doi: 10.1061/(ASCE)1084-0699(2005)10:3(243)CE.
Merwade, V. M., D. R. Maidment, and J. A. Goff (2006), Anisotropic considerations while interpolating river channel bathymetry, *J. Hydrol.*, *331*(3), 731–741, doi:10.1016/j.jhydrol.2006.06.018.
Merwade, V., A. Cook, and J. Coonrod (2008), GIS techniques for creating river terrain models for hydrodynamic modeling and flood inundation mapping, *Environ. Model. Software*, *23*(10), 1300–1311, doi:10.1016/j.envsoft.2008.03.005.
Merwade, V. (2009), Effect of spatial trends on interpolation of river bathymetry, *J. Hydrol.*, *371*(1), 169–181, doi:10.1016/j.jhydrol.2009.03.026.
Neal, J. C., P. D. Bates, T. J. Fewtrell, N. M. Hunter, M. D. Wilson, and M. S. Horritt (2009), Distributed whole city water level measurements from the Carlisle 2005 urban flood event and comparison with hydraulic model simulations, *J. Hydrol.*, *368*(1), 42–55, doi:10.1016/j.jhydrol.2009.01.026.
Neal, J., G. J. P. Schumann, and P. D. Bates (2012a), A subgrid channel model for simulating river hydraulics and floodplain inundation over large and data sparse areas, *Water Resour. Res.*, *48*, W11506, doi:10.1029/2012WR012514.
Neal, J., I. Villanueva, N. Wright, T. Willis, T. Fewtrell, and P. D. Bates (2012b), How much physical complexity is needed to model flood inundation?, *Hydrol. Processes*, *26*(15), 2264–2282, doi:10.1002/hyp.8339.
Nguyen, P., A. Thorstensen, S. Sorooshian, K. Hsu, A. AghaKouchak, B. Sanders, V. Koren, Z. Cui, and M. Smith (2015), A high resolution coupled hydrologic–hydraulic model (HiResFlood-UCI) for flash flood modeling, *J. Hydrol.*, *541*, 401–420, doi:10.1016/j.jhydrol.2015.10.047.
Nicholas, A. P., and G. H. Sambrook Smith (1999), Numerical simulation of three-dimensional flow hydraulics in a braided channel, *Hydrol. Processes*, *13*(6), 913–929, doi:10.1002/(SICI)1099-1085(19990430)13:6<913::AID-HYP764>3.0.CO;2-N.
Nicholas, A. P., et al. (2012), Modelling hydrodynamics in the Rio Paraná, Argentina: An evaluation and inter-comparison of reduced-complexity and physics based models applied to a large sand-bed river, *Geomorphology*, *169*, 192–211, doi:10.1016/j.geomorph.2012.05.014.
Osting, T. D. (2004), An improved anisotropic scheme for interpolating scattered bathymetric data points in sinuous river channels, report 04-01, Cent. Res. Water Resour., Univ. of Austin, Tex.
Paiva, R. C. D., W. Collischonn, and C. E. M. Tucci (2011), Large scale hydrologic and hydrodynamic modeling using limited data and a GIS based approach, *J. Hydrol.*, *406*(3), 170–181, doi:10.1016/j.jhydrol.2011.06.007.
Paiva, R. C. D., W. Collischonn, and D. C. Buarque (2013), Validation of a full hydrodynamic model for large-scale hydrologic modelling in the Amazon, *Hydrol. Processes*, *27*(3), 333–346, doi:10.1002/hyp.8425.
Pavelsky, T. M., and L. C. Smith (2008), RivWidth: A software tool for the calculation of river widths from remotely sensed imagery, *IEEE Geosci. Remote Sens. Lett.*, *5*(1), 70–73, doi:10.1109/lgrs.2007.908305.
Sampson, C. C., A. M. Smith, P. D. Bates, J. C. Neal, L. Alfieri, and J. E. Freer (2015), A high-resolution global flood hazard model, *Water Resour. Res.*, *51*, 7358–7381, doi:10.1002/2015WR016954.
Schubert, J. E., W. W. Monsen, and B. F. Sanders (2015), Metric-resolution 2D river modeling at the macroscale: Computational methods and applications in a braided river, *Front. Earth Sci.*, *3*, 74, doi:10.3389/feart.2015.00074.
Schumann, G. J. P., P. D. Bates, J. C. Neal, and K. M. Andreadis (2014a), Fight floods on a global scale, *Nature*, *507*(7491), 169–169.
Schumann, G. J. P., K. M. Andreadis, and P. D. Bates (2014b), Downscaling coarse grid hydrodynamic model simulations over large domains, *J. Hydrol.*, *508*, 289–298, doi:10.1016/j.jhydrol.2013.08.051.
Schumann, G. J. P., D. Stampoulis, A. M. Smith, C. C. Sampson, K. M. Andreadis, J. C. Neal, and P. D. Bates (2016), Rethinking flood hazard at the global scale, *Geophys. Res. Lett.*, *43*, 10,249–10,256, doi:10.1002/2016GL070260.
Smith, J. D., and S. R. McLean (1984), A model for flow in meandering streams, *Water Resour. Res.*, *20*(9), 1301–1315, doi:10.1029/WR020i009p01301.
Surian, N. (2015), Fluvial processes in Braided rivers, in *Rivers-Physical, Fluvial and Environmental Processes*, pp. 255–277, Springer International Publishing, Switzerland, doi:10.1007/978-3-319-17719-9_15.
Toniolo, H. (2013), Bedforms andsediment characteristics along the thalweg on the Tanana River near Nenana, Alaska, USA, *Nat. Resour.*, *4*, 20–30, doi:10.4236/nr.2013.41003.
Toniolo, H., P. Duvoy, S. Vanlesberg, and J. Johnson (2010), Modelling and field measurements in support of the hydrokinetic resource assessment for the Tanana river at Nenana, Alaska, *Proc. Inst. Mech. Eng. A, J. Power Energy*, *224*(8), 1127–1139, doi:10.1243/09576509JPE1017.
Williams, R. D., J. Brasington, M. Hicks, R. Measures, C. D. Rennie, and D. Vericat (2013), Hydraulic validation of two-dimensional simulations of braided river flow with spatially continuous aDcp data, *Water Resour. Res.*, *49*, 5183–5205, doi:10.1002/wrcr.20391.
Yamazaki, D., S. Kanae, H. Kim, and T. Oki (2011), A physically based description of floodplain inundation dynamics in a global river routing model, *Water Resour. Res.*, *47*, W04501, doi:10.1029/2010WR009726.
Ziliani, L., N. Surian, T. J. Coulthard, and S. Tarantola (2013), Reduced-complexity modeling of braided rivers: Assessing model performance by sensitivity analysis, calibration, and validation, *J. Geophys. Res. Earth Surf.*, *118*, 2243–2262, doi:10.1002/jgrf.20154.